



2nd Advanced Optical Metrology Compendium

Advanced Optical Metrology

Geoscience | Corrosion | Particles | Additive Manufacturing: Metallurgy, Cut Analysis & Porosity



EVIDENT
OLYMPUS

WILEY

The latest eBook from **Advanced Optical Metrology**.
Download for free.

This compendium includes a collection of optical metrology papers, a repository of teaching materials, and instructions on how to publish scientific achievements.

With the aim of improving communication between fundamental research and industrial applications in the field of optical metrology we have collected and organized existing information and made it more accessible and useful for researchers and practitioners.

EVIDENT
OLYMPUS

WILEY

3D-Printed Soft and Hard Meta-Structures with Supreme Energy Absorption and Dissipation Capacities in Cyclic Loading Conditions

Armin Yousefi, Saman Jolaiy, Mohammadreza Lalegani Dezaki, Ali Zolfagharian, Ahmad Serjouei, and Mahdi Bodaghi*

The main objective of this article is to introduce novel 3D bio-inspired auxetic meta-structures printed with soft/hard polymers for energy absorption/dissipation applications under single and cyclic loading–unloading. Meta-structures are developed based on understanding the hyper-elastic feature of thermoplastic polyurethane (TPU) polymers, elastoplastic behavior of polyamide 12 (PA 12), and snowflake inspired design, derived from theory and experiments. The 3D meta-structures are fabricated by multi-jet fusion 3D printing technology. The feasibility and mechanical performance of different meta-structures are assessed experimentally and numerically. Computational finite element models (FEMs) for the meta-structures are developed and verified by the experiments. Mechanical compression tests on TPU auxetics show unique features like large recoverable deformations, stress softening, mechanical hysteresis characterized by non-coincident compressive loading–unloading curve, Mullins effect, cyclic stress softening, and high energy absorption/dissipation capacity. Mechanical testing on PA 12 meta-structures also reveals their elastoplastic behavior with residual strains and high energy absorption/dissipation performance. It is shown that the developed FEMs can replicate the main features observed in the experiments with a high accuracy. The material-structural model, conceptual design, and results are expected to be instrumental in 3D printing tunable soft and hard meta-devices with high energy absorption/dissipation features for applications like lightweight drones and unmanned aerial vehicles (UAVs).

1. Introduction

Today reducing the weight of structures while maintaining the main features and enhancing them is a constant need in developing advanced structures. One common solution for achieving these goals is developing sandwich structures consisting of three main parts, two face sheets, and the central core. The geometry and materials of the sandwich are an area that has been extensively investigated by numerous researchers.^[1–3] Recently, metamaterials have been introduced successfully. These structures exhibit negative Poisson's ratio (NPR) under compression or tension loads, also known as auxetic structures.^[4,5] In 1991, the term “auxetic” was used for these types of structures for the first time.^[6] The innovation of auxetic structures arises from their geometrical properties, which show an unusual reaction to the applied load. They expand or contract when axially stretched or compressed.^[5,7] These materials exhibit special properties over conventional materials, better energy absorption/impact resistance, and unique acoustic energy absorption capabilities. One of

the unique properties of auxetic structures is their high energy absorption per mass of structures, known as specific energy absorption (SEA). Several studies have attempted to develop novel auxetic structures with higher energy absorption capability while lower overall mass.^[8–14] These superior features offer a wide range of smart filters, sensors, medical devices, and protective equipment applications. Due to their superior properties, they are potential candidates to use as energy-absorbing structures for a wide range of industries. This includes areas that require explosion reduction such as military vehicle undercarriage and explosion-proof vests. They are highly usable in the impact resistance applications, such as car bumpers, accident-prone structures, or sports protective gears such as sports mats and helmets. In addition, these structures due to high SEA are highly recommended for aerospace applications in which weight reduction is crucial. For example, in aerospace structures construction such as aircraft nose components.^[15–19]

3D printing is one of the best processes to make auxetic structures. 3D printing is a procedure to create an object of any shape

A. Yousefi, S. Jolaiy, M. Lalegani Dezaki, A. Serjouei, M. Bodaghi
Department of Engineering
School of Science and Technology
Nottingham Trent University
Nottingham NG11 8NS, UK
E-mail: mahdi.bodaghi@ntu.ac.uk

A. Zolfagharian
School of Engineering
Deakin University
Geelong 3216, Australia

 The ORCID identification number(s) for the author(s) of this article can be found under <https://doi.org/10.1002/adem.202201189>.

© 2022 The Authors. Advanced Engineering Materials published by Wiley-VCH GmbH. This is an open access article under the terms of the Creative Commons Attribution License, which permits use, distribution and reproduction in any medium, provided the original work is properly cited.

DOI: 10.1002/adem.202201189

by continuously placing the designed material under computer control. 3D printing makes it possible to manufacture novel and complex structures in a reasonable amount of time compared to conventional manufacturing processes. It provides opportunities for precise, cost-effective, and time-saving manufacturing of auxetic structures with a wide range of materials,^[20–22] primarily polymers, due to ease of 3D printing, cost-effectiveness, lightness, and flexibility. Auxetic structures are usually achieved by designing specific structures consisting of periodically arranged auxetic unit cells. These structures are divided into different categories based on deformation and geometry. Chiral structures, re-entry structures, rotating rigid structures, origami, and kirigami-based materials, perforating structures, and auxetic foams are common forms of these structures. Recent studies have introduced new auxetic structures and discussed their topological optimization for effective Young's modulus and capability of higher energy absorption. The interaction of geometric parameters such as the ratio of base length and connection angle on the hardness, strength, and energy absorption properties of re-entrant auxetic honeycombs as a common type of auxetic structures was evaluated.^[23–25]

It should be mentioned that most 3D auxetic structures have 2D patterns developed and printed in the third dimension. Several researchers have investigated the different properties of various 2D-extended auxetic structures under loading–unloading conditions. For example, Bodaghi et al.^[26] introduced novel auxetic sandwich structures consisting of soft and hard materials and investigated the energy absorption capability for one loading–unloading cycle. The results showed that the proposed auxetic structures can be fully recovered by simply heating them. Mehrpouya et al.^[27] investigated the effect of printing parameters such as printing speed and nozzle diameter on the reversibility of polylactic acid (PLA) sandwich structures. Results showed that by decreasing the printing speed and increasing nozzle size, the shape recovery feature of structures is enhanced. Serjouei et al.^[28] examined the energy absorption and shape recovery capability of two bio-inspired horseshoe-shaped structures with a negative Poisson's ratio under the mono loading–unloading cycle. The effect of different manufacturing parameters on the energy absorption and shape recovery of the proposed sandwich structures was investigated. The SEA was reported for different models and configurations. Results revealed that by increasing the thickness of structures, although the mass is increased, the energy absorption rate becomes much more considerable, enhancing the SEA. Recently, Hamzehie^[29] introduced zero Poisson's ratio hard meta-materials with reversible energy-absorbing features fabricated by 4D printing technology. The deformation could be recovered by simply heating.

In recent years, extensive research has been done to design and develop meta-structures from natural or biological structures for different purposes, from enhancing energy absorption to thermal conductivity.^[14,30–34] For instance, Hamzehei et al.^[30] introduced zero Poisson's ratio meta-materials based on the DNA molecule for energy absorption applications. Saufi et al.^[35] studied the energy absorption capability of 3D-printed bio-inspired honeycomb structures reinforced by starfish shape elements.

As the literature review shows, most of the research focus has been on developing 2D meta-structure patterns and extending them into the third dimension. 3D soft and hard auxetic structures are yet to be developed, and 3D printing and their

capabilities in absorbing and dissipation energies in single and cyclic loadings should be explored.

The present work aims to introduce novel 3D bio-inspired auxetic meta-structures printed with soft and hard polymers and investigate their energy absorption and dissipation capacities under single and cyclic loading–unloading conditions. The conceptual design is based on arranging snowflake-inspired unit cells of soft recoverable thermoplastic polyurethane polymers and elastoplastic hard polyamide 12 (PA 12) polymers. Thermoplastic polyurethane (TPU) is widely used in the production of soft actuators, vibration resistance, smart wearable devices, energy storage, and biomedical devices.^[36] Novel 3D auxetics and material samples are 3D printed by multi-jet fusion (MJF) technology and tested mechanically. Experimental tests show the capability of soft TPU materials to undergo large deformations with a high shape recovery feature. Their behavior exhibits stress softening, hysteresis, cyclic stress softening, and high energy absorption/dissipation. Mechanical testing on PA 12 auxetics also reveals their elastoplastic behavior with some residual strains and super energy absorption/dissipation performance. A finite element model (FEM) via ABAQUS software is developed to predict the nonlinear responses of auxetic structures. Hyperelastic and elastoplastic models are assumed to model soft and hard polymers. The Mullins effect and fracture model are also considered to enhance the accuracy of modeling soft and hard polymers in the large strain range. Numerical simulations using ABAQUS FEM are implemented to predict the results of experiments on mechanical loading–unloading in a monotonic and cyclic manner. It is observed that the nonlinear compressive softening/hardening stress, plateau stress, hysteresis, cyclic stress softening, Mullins effect, and energy absorption/dissipation capacity of meta-structures can be replicated accurately by the simulations. The material-structural model, concepts, and experimental/numerical results provided in this article are expected to open an avenue for the design and implementation of energy absorption and dissipating meta-devices by harnessing hyperelasticity, elastoplasticity, and mechanical instability.

Figure 1 shows the different steps from the bio-inspired design to the application of the proposed meta-structure. In step 1, the unit cell shape is inspired by snowflakes which have star-shaped patterns. The proposed novel 3D auxetic meta-structures are developed from the unit cell following the way snowflakes' edges are connected to each other. In step 2, the proposed meta-structure is 3D printed by employing the MJF method. In step 3, computational tools along with experimental setup are developed to test and understand the mechanical behaviors of the designed meta-structures. In the final step, their mechanical performance is examined for low-velocity impact protection applications. For instance, as shown in Figure 1, drones have delicate components like camera and/or transport delicate goods and their arms and landing gears experience low-velocity impacts during landing and collision. The energy-dissipating meta-structures proposed in this work could be instrumental in designing such lightweight drones. Nowadays unmanned aerial vehicles (UAVs) are also 3D printed, for instance, Aurora and Stratasy have 3D printed honeycomb-based lattices for UAV wings,^[37] and our proposed energy-absorbing meta-structures could be insightful in designing internal structures of UAV wings.

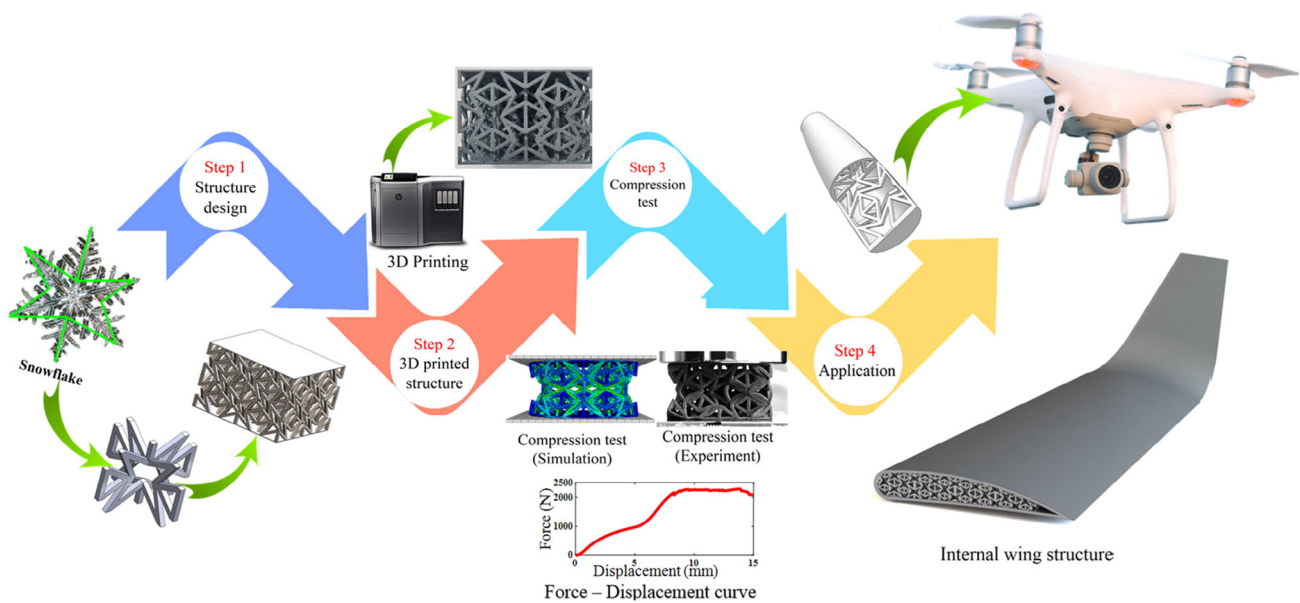


Figure 1. Different steps, from design to application of novel 3D auxetic structure.

2. Experimental Section

2.1. Materials and 3D Printing

The process used to fabricate the lattice-based energy absorbers is MJF, which is a powder bed fusion additive manufacturing technique. MJF, introduced in 2014, is a proprietary technology of Hewlett-Packard (HP) Inc. MJF uses an inkjet array to selectively apply fusing and detailing agents across a bed of polymer powder. The fusing agent was deposited by inkjet nozzles installed in a carriage to the targeted regions of the powder bed at the voxel level. In contrast, a water-based detailing agent was jetted around the contours of the printed parts to inhibit the fusion of powder near the part edges and to improve part resolution. An array of infrared lamps then fused them into a solid. Once a layer was built, a fresh layer of powder was distributed on top of the previous layer, and the following phase continued until the object was fully completed. The biggest advantage of MJF was that no support material is needed, which means complicated 3D lattices can be designed without having to build supports. This frees up design potential in this work. Before 3D printing the object, the design was created by SOLIDWORKS software and then converted to STL file format to be imported into the MJF 3D printer.

The meta-structures were assumed to be 3D printed with soft and hard components with hyper-elastic and elastoplastic features. TPU powder was considered a soft elastomer, while PA 12 powder was selected as a hard material. To obtain mechanical properties of the soft and hard materials, 5 cylinders and 5 dog-bone specimens were 3D printed via MJF based on the dimensions and geometry of ASTM D695^[38] and ASTM D638 (Type IV, 2 mm thickness),^[39] respectively.

Uniaxial compressive and tensile tests were carried out on cylinder and dog-bone specimens by means of Shimadzu R AGS-X 50 kN (Kyoto, Kyoto Prefecture, Japan). This is a universal

machine equipped with a 1 kN load cell, and samples were tested mechanically at room temperature ≈ 23 °C with a speed of 1 mm min^{-1} in a quasi-static manner. The Trapezium X software was also employed as a visual wizard that provides guidance for setting control parameters such as test speed, load capacity, and gauge sensors. Shimadzu offered TRViewX (TRViewX Digital Video Extensometer, Japan) noncontact digital video extensometer. The gauge marks on dog-bone samples were monitored and tracked to measure the strain of the specimens by TRViewX integrated with the Trapezium X.

The uniaxial tensile results in terms of stress-strain for all specimens were considered acceptable due to consistency. The experimental stress-strain responses for TPU and PA 12 are illustrated in **Figure 2a,b**, respectively. Figure 2a shows that the soft TPU behaves in a nonlinear super-elastic manner. Initial loading follows path A up to point P, and subsequent unloading follows path B, which lies below A. As loading and unloading paths in the first cycle do not coincide, a hysteresis loop appears when unloading. This stress softening mechanism is characterized by a decrease in the stress on unloading compared to the stress on loading at the same strain. It is also seen that the soft material is able to undergo large deformations and recover to the initial shape without any residual strain. TPU mechanical behavior is further investigated via the second loading-unloading cycle. Reloading to the strain P follows the new path C, which lies between A and B. Subsequent unloading from P to 0 follows almost path B. The second cyclic loading in Figure 2a reveals that TPU presents a loss of stiffness, leading to cyclic stress softening and stress hysteresis. This phenomenon is well known as the Mullins effect.^[40]

Next, the mechanical behavior of PA 12 is examined. Figure 1b reveals that PA 12 has a linear behavior in the beginning before 35 MPa stress, followed by a nonlinear hardening plasticity till the break-down point ($\approx 20\%$ strain). Figure 2b shows that the PA 12 experiences a low slope plateau during plastic deformation

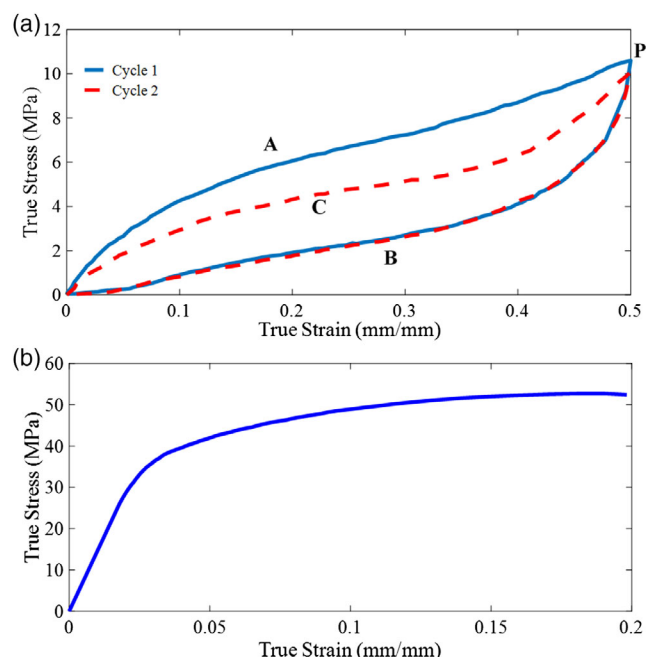


Figure 2. Stress–strain response of experimental compressive and tensile tests of: a) thermoplastic polyurethane (TPU) and b) polyamide 12 (PA 12) samples.

growth. As the strain rate is very low, the material behavior can be considered elastoplastic.

2.2. Conceptual Design

In the design part, extensive research has been done to design novel 3D auxetic structures with an acceptable NPR representing auxeticity. The aim is to have a high energy absorption capability with a lower mass. The result of design trials was a novel bio-inspired 3D star-triangular auxetic honeycomb (3DSTH) made of a unique unit cell, developed via SOLIDWORKS software as presented in Figure 3a. As presented in Figure 3a, the strut thickness is 2 mm. This auxetic design was enhanced and optimized based on the star-triangular auxetic honeycomb (STH) and inspired by star-shaped snowflakes. STH design shows selective mechanical properties and stability during large deformations compared to conventional auxetic structures (re-entrant, double-arrow, and star structures).^[41,42] Moreover, the star-shaped snowflakes and how snowflakes' edges are connected to each other inspire designing such meta-structures. The present study proposes a novel 3D auxetic structures based on the 3DSTH unit cell to enhance the energy absorption per unit mass, see Figure 3b.

3. Finite Element Modeling

3.1. Material and Loading Setting

The present study examines the novel auxetic structures under cyclic loading numerically and experimentally. Auxetic structures are drawn in SOLIDWORKS software, and modeled in the

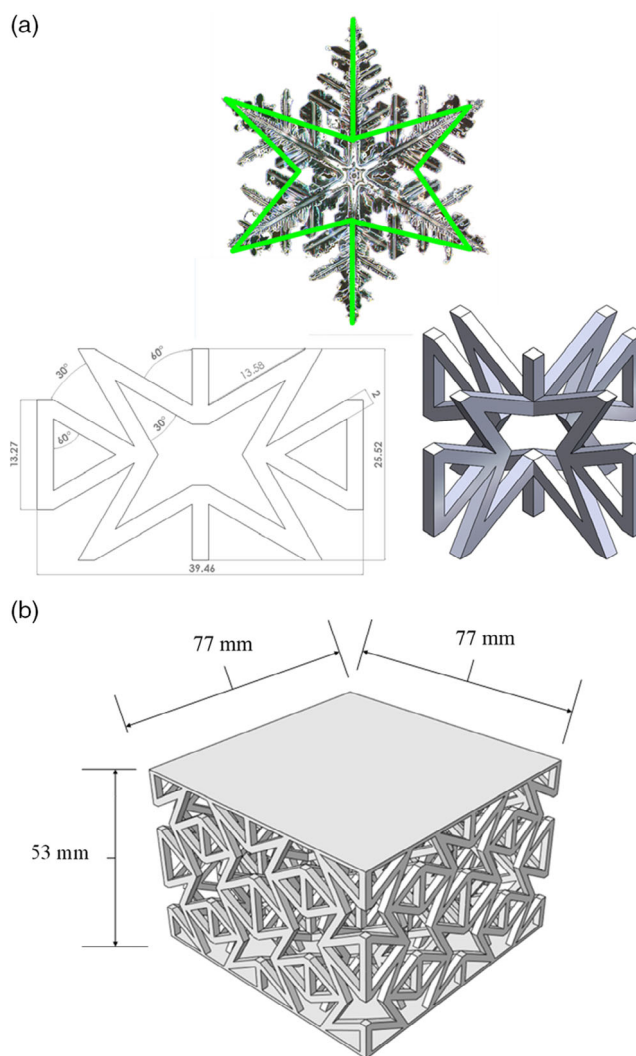


Figure 3. Novel 3DSTH structures: a) bio-inspired unit cell with (all dimension units are in millimeters), b) 3D model.

ABAQUS software package (V.6.14, Dassault Systems, France) as parts considering two different materials, PA 12 and TPU, the same as the experimental study. Due to the complexity of structures and high numbers of elements that should be used to mesh auxetic structures, Dynamic Explicit is considered to model structures with less computing time. Dynamic Explicit solutions are recommended for complex structures due to lower computing time and their ability to solve complex problems efficiently. To define Dynamic Explicit in ABAQUS, first, in the step modulus, the Dynamic Explicit option is selected. After that, the option NLgeom is considered, accounting for geometric nonlinearity in that step. In addition, the type Fixed and Global in the increment estimator is selected in the increment section. When the Dynamic Explicit is selected, in the load modulus, Amplitude option must be selected; in the present research, the Tabular is chosen.

To assign the mechanical properties of materials, the experimental stress–strain data is imported to ABAQUS using the

calibration option. ABAQUS fits the curve of the experimental data; then, the mechanical properties are created and assigned to the parts depending on the behavior of materials selected by users.

In the present study, to simulate the PA 12 auxetic structure, an elastic–plastic model is considered to replicate the experimental behavior of PA 12. For modeling the TPU structures, Mooney–Rivlin hyperelastic model^[43] is used regarding the cyclic behavior of cylindrical samples, which is presented in Figure 2. The Mooney–Rivlin parameters are determined by using Evaluate Materials option in ABAQUS ($C_{10} = -2.8969$, $C_{01} = 11.2283$, $D_1 = 0$). Another important feature of the present model is to consider the Mullins effect in the simulation. The rubber materials under large deformation conditions exhibit unique properties, which are cyclic stress softening known as the Mullins effect. One of the Mullins effect's fundamental assumptions is that the next cycle's loading has the same unloading path as the previous cycle.^[40,44] The ABAQUS software has the capability to consider the Mullins effect based on the experimental data. Using the Mooney–Rivlin model, the hyperelastic behavior of TPU is first modeled. Then, the Mullins effect is used to model how TPU softens when it is deformed

A meshed auxetic structure modeled in the present study is illustrated in **Figure 4a**. The model consists of three main parts, upper movable jaw, auxetic structure, and fixed jaw. The upper and lower body is considered rigid to simulate the compression test better. ABAQUS uses two primary methods to define parts as a rigid body. The first method is the part modulus when the part is defined, and the second method is in the interaction modulus when the constraint is defined. In the present study, the second method is employed to determine the rigid body; so the reference point is set, and the upper and lower reaction force and displacement can be easily exported. To model the cyclic loading, two steps are defined for each cycle. In the first step, loading, the upper jaw moves in the negative Y direction (compression

loading) and stops at a specified displacement (same as the experimental test). In the second step, unloading, the upper jaw moves back in the Y direction to the initial position. The reaction force and displacement are recorded for the upper jaw. General contact is defined between different parts in both normal and tangential directions.

The mesh refinement technique is also examined to gain more reliable results while reducing computing time as much as possible. Figure 4b shows the mesh refinement technique results for the loading section of the analysis for TPU materials. In the present study, various elements are applied to check the mechanical behavior of the meta-structure. As can be seen, 30 000 elements (Linear tetrahedron, type C3D4) result in a coverage force–displacement trend, and at least this number of elements are chosen for all simulation efforts. Linear hexahedron elements, type C3D8R are used to mesh upper and lower jaws.

4. Results and Discussion

4.1. Experimental and Numerical Results for TPU

This section reports the different stages of loading–unloading for 3D-printed TPU auxetic structures. Two different samples named sample 1 and sample 2 are printed and tested subjected to a maximum strain of 50% and 25%, respectively. **Figure 5a–g** presents various stages of the TPU auxetic structure (sample 1) under loading/unloading cycles for cycle 1 and force–displacements curves for cycles 1 and 2 with a maximum strain of almost 50%. Figure 5a shows the starting step when the structure is in the rest condition. Figure 5b represents the auxetic structure for the strain of 50% (the maximum displacement of 25 mm). As presented in Figure 5b,c, the structure does not fail and recover at even large deformations due to the super-elastic properties of hyper-elastic TPU. It is seen that the structure does not fully recover to the initial shape and some residual strain and distortion remain in the structure. Residual strain is due to some irrecoverable plastic deformations. Figure 5d–f presents the FEM simulation results. As illustrated in these figures, the FEM predicts the deformation of the structure with a good accuracy compared to the experimental results. Comparing Figure 5b,e shows that although the structure is symmetric, the left edges of the structure are more deformed than the right edges, proving that the present model can simulate deformations with high accuracy. This phenomenon is observed only in TPU auxetic structure due to large deformation bifurcation-type buckling while the deformation is completely symmetric in the PA 12 meta-structure with less deformation. The current model even predicts the unloading details very well. The stress contour shows that some stress remains in the structures after unloading due to residual strain and local distortion. By focusing on Figure 5g for the force–displacement of sample 1 (50%) under cycles 1 and 2, it is found that FEM can replicate experimental results during cycles. It proves the Mooney–Rivlin model's capability and the Mullins effect in predicting experimental observations.

At the first stage of loading (0–2.5 mm) in cycle 1, the load versus displacement has a linear trend. The V-shaped beam-like elements start to bend exactly at the middle line. Between displacement of 5–8 mm, the beam-like elements at the middle line contact each other, and the load increases at a higher rate than

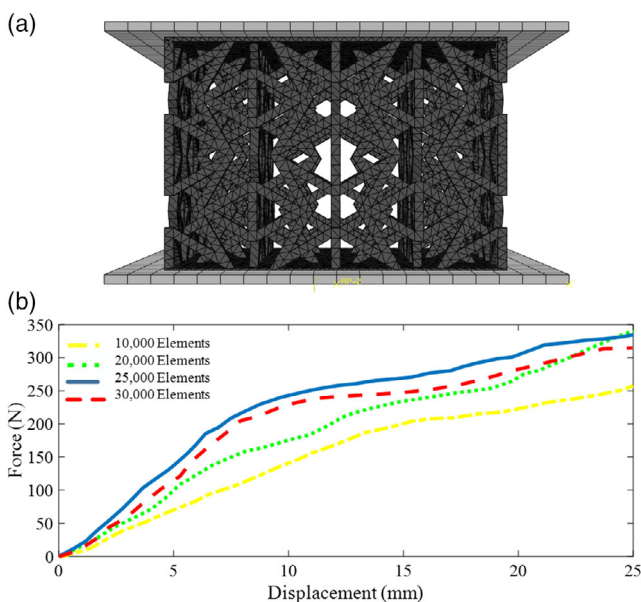


Figure 4. a) A meshed auxetic structure and b) mesh refinement results.

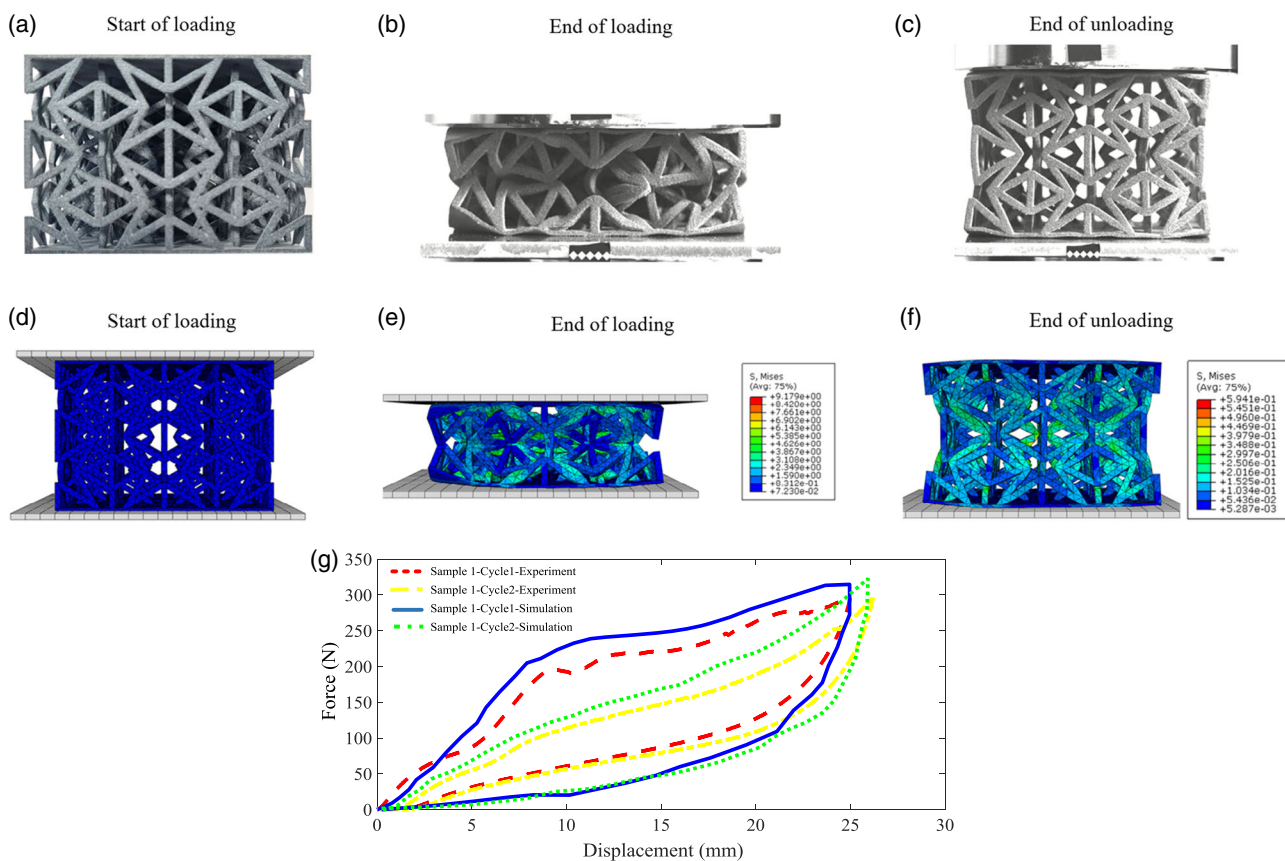


Figure 5. Different stages of TPU sample 1 for applied maximum 50% strain in cycle 1: a) start of loading (experiment), b) end of loading (experiment), c) end of unloading (experiment), d) start of loading (simulation), e) end of loading (simulation), f) end of unloading (simulation); g) force-displacements curves for cycles 1 and 2 obtained from experiment and simulation.

displacement. Between displacement of 8–18 mm, the plateau regime can be seen (with a slight slope) in which the displacement increases at a high rate almost at the same load. That is due to the softening behavior of the material. Between displacement of 18 and 25 mm, densification occurs in which the slope of load versus displacement increases. Afterward, the unloading occurs, and the structure tends to recover its initial shape. Loading and unloading paths do not coincide, making a hysteresis loop resulting in energy dissipation. It is seen that the structure cannot fully recover its initial form, and the height of the final and initial structure has a difference of almost 2 mm. After unloading in cycle 1, cycle 2 is started. In cycle 2, same as cycle 1, 50% strain is applied to the structure. In the first stage, the loading is applied. Due to a loss of stiffness (Mullins effect), the force-displacement curve in cycle 2 is different from its counterpart in cycle 1. As discussed before, the Mullins effect is considered for the simulation based on the TPU experimental results, so the load–displacement predicted by FEM is very close to the experimental one. A decrease in the stress hysteresis width from cycle 1 to cycle 2, cyclic stress softening, and similar unloading paths are observed that are predicted with FEM very well. Comparing the results from FEM and experiments reveal that the model overestimates the stress hysteresis width due to considering perfect initial geometries and pure

hyper-elasticity. Like the previous cycle, the structure cannot fully recover, so in cycle 2 the final residual displacement is higher than in the previous cycle (almost 2 mm) due to an accumulation of plastic deformations. It is worth mentioning that after unloading in cycle 2, the difference between the initial form of the auxetic structure and the final form (cycle 2) is more prominent.

Figure 6a–g shows the mechanical behavior of 3D-printed TPU auxetic structure for 25% strain (sample 2) under two loading–unloading cycles. The counterpart of Figure 5 for the present example is demonstrated in Figure 6. As can be concluded from this figure, the developed FEM can replicate the experiments very well. Comparing the final form of sample 2 with that of sample 1 shows that sample 2 recovers better than the initial form and has a higher shape recovery capability. The main reason is that in sample 2, the maximum displacement is 25% less than sample 1, so the residual strain is less and subsequently, the distortion is less than sample 1. Figure 6b,e clearly reveal the auxeticity feature of the structure, with an obvious shrinkage in the middle line. As in sample 1, at starting of the loading part, the load versus displacement curve is linear. After that, the beam-like structure near the middle line starts to buckle and contact each other, and the load versus displacement slope increases. At displacement between 8 and 12.5 mm, a plateau regime occurs when the displacement

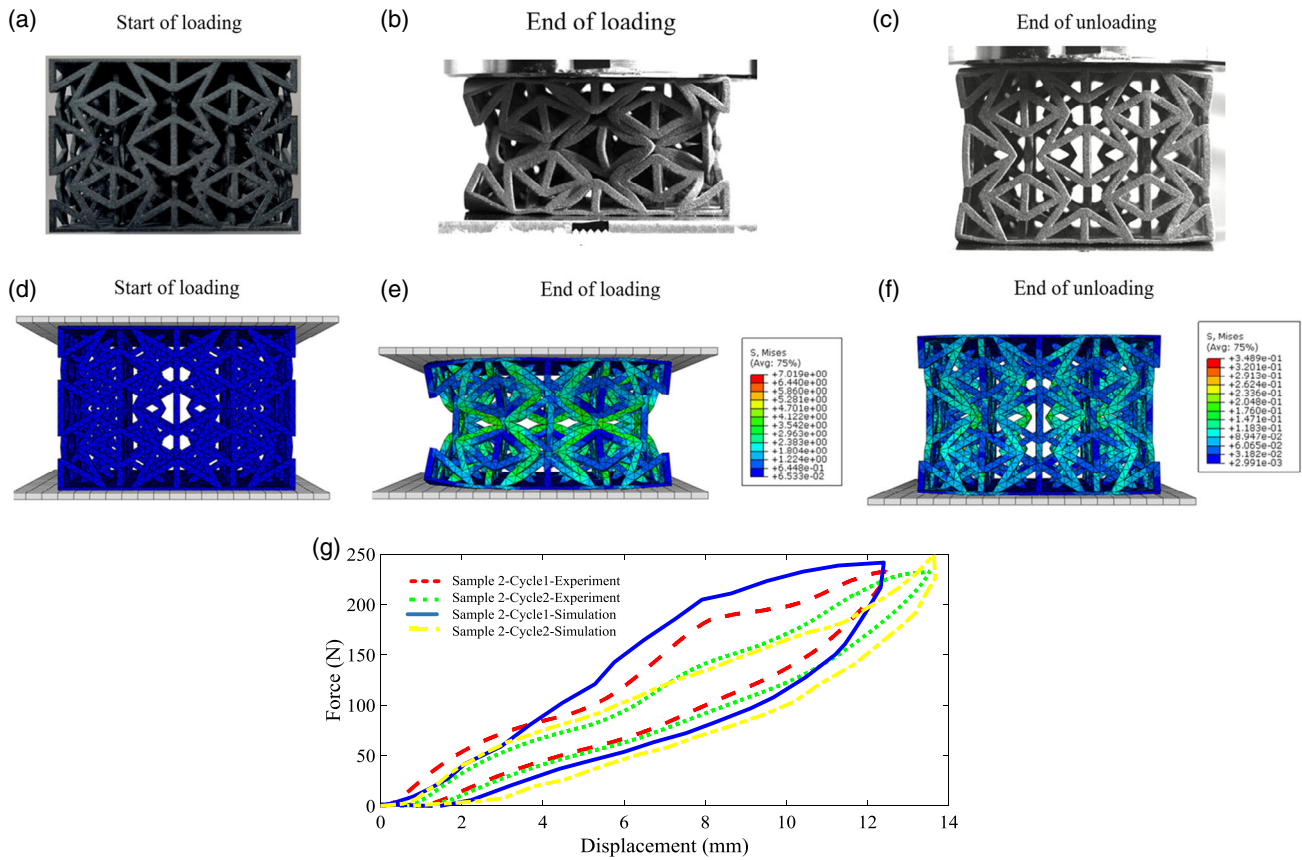


Figure 6. Different stages of TPU sample 2 for 25% strain: a) start of loading (experiment), b) end of loading (experiment), c) end of unloading (experiment), d) start of loading (simulation), e) end of loading (simulation), f) end of unloading (simulation); g) force-displacements curves for cycles 1 and 2 obtained from experiment and simulation.

increases along with a very low increase in the load. The load–displacement curve in the unloading section is closer to the loading stage compared to sample 1 reducing the width of the hysteresis loop. When the movable jaw separates from the structure (0 N) because of the residual strain, the structure height reads almost 1.7 mm shorter in comparison with the initial shape. After unloading in cycle 1, the load is applied in cycle 2. It is worth mentioning that because of the Mullins effect, the load at the specified displacement is less than cycle 1. Also, the hysteresis loop of cycle 2 is smaller than the hysteresis loop of cycle 1.

Figure 7 displays an isometric view of the meta-structure in different loading–unloading stages for the strain of 50% (sample 1, cycle 2). As the proposed structure is a 3D auxetic meta-structure, it is observed that the meta-structure provides unique properties such as NPR along all faces.

4.2. Dissipated and Absorbed Energies, and SEA for TPU

Another critical parameter being investigated here is the energy distribution of auxetic structures. Dissipated energy and energy absorption are essential parameters of auxetic structures. **Figure 8** presents the energy graph of an auxetic structure (experimental results of sample 1 for cycle 1), highlighting the

area under force–displacement. The total energy applied to auxetic structures is divided into dissipated and absorbed energies. Dissipated energy is the area between the loading–unloading versus displacement curve. Meanwhile, the absorbed energy is the amount of energy under the unloading–displacement curve. It is worth mentioning that when the structures reach failure load, the area under the loading–displacement curve defines energy absorption. The absorbed energy is the kinetic energy required for the elastic deformation of structures, and dissipated energy is the energy due to residual strain or instability in the structure. The energy dissipation and absorption for all loading–unloading curves of samples 1 and 2 at cycles 1 and 2 are calculated in **Table 1**. Another critical parameter that considers energy dissipated and the structure’s mass is SEA, which is defined as follows

$$SEA = \frac{\text{Dissipated Energy per cycle}}{\text{Mass}} \quad (1)$$

According to Equation (1), the SEA is directly related to the red area of the energy graph. It is worth mentioning that SEA is defined as absorbed energy per unit mass in some open literature which is similar to the present definition. SEA is the amount of energy dissipated by structures due to plastic deformation and

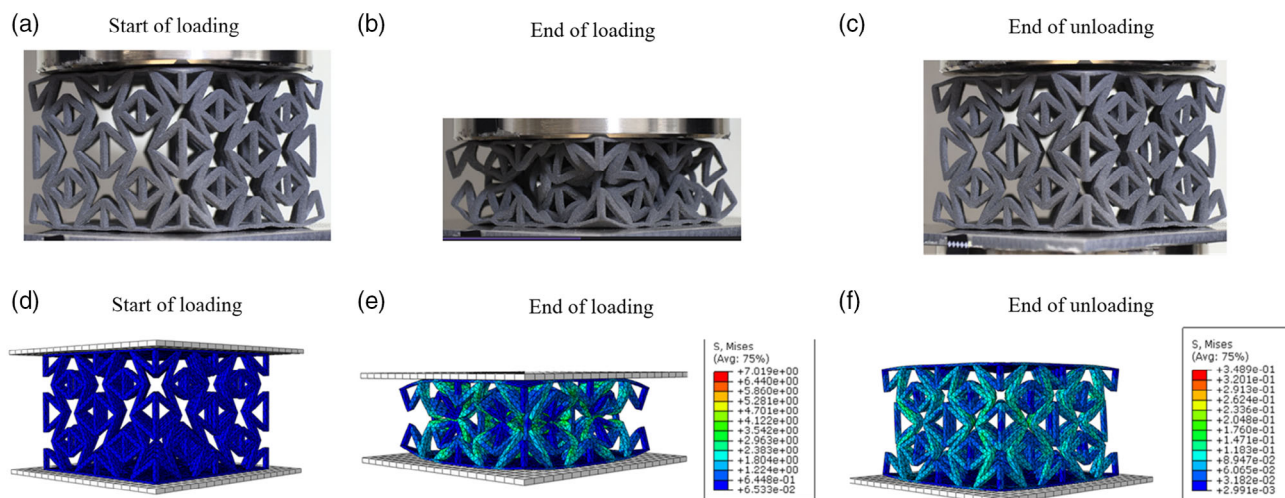


Figure 7. Isometric views of the TPU auxetic structure under the loading–unloading process for the strain of 50%: a) start of loading (experiment), b) end of loading (experiment), c) end of unloading (experiment), d) start of loading (simulation), e) end of loading (simulation), f) end of unloading (simulation).

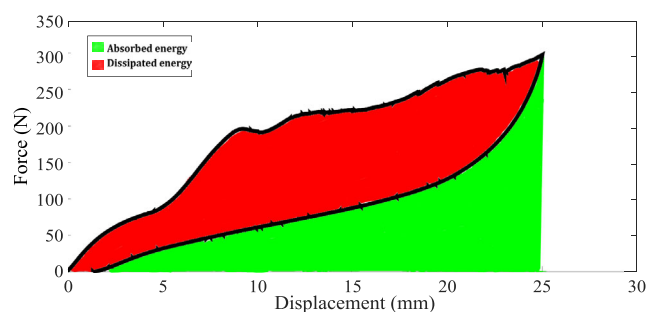


Figure 8. Absorbed and dissipated energy distribution.

Table 1. Dissipated energy, absorbed energy, and SEA for TPU samples 1 and 2 at cycles 1 and 2.

Sample/Cycle	Dissipated energy [J]	Absorbed energy [J]	SEA [J g]
Sample 1/Cycle 1	2.552	2.103	0.0543
Sample 1/Cycle 2	1.397	2.095	0.0297
Sample 2/Cycle 1	0.599	1.018	0.0127
Sample 2/Cycle 2	0.444	1.122	0.0094

instability per unit mass in the present study. When the deformation in the structure is entirely in the elastic regime, the SEA becomes zero. Also, when structures are subjected to a load leading to failure, the area under force–displacement per unit mass defines the SEA.

The dissipated energy, absorbed energy, and SEA for TPU for two samples and two cycles are listed in Table 1. As can be seen, the dissipated energy and SEA for sample 1/cycle 1 are higher than sample 1/cycle 2 by 83%, which means that the structure in the first cycle dissipates more energy than cycle 2 due to cyclic softening. Also, the dissipated energy and SEA for sample 2/cycle 1 are higher than sample 2/cycle 2 by 35%. The SEA for

sample 1/cycle 1 is 328% higher than sample 2/cycle 1 because sample 1 is subjected to larger displacement, and more energy is dissipated by sample 1. The SEA for sample 1 in both cycles is 0.084 J g^{-1} , while for sample 2 is 0.0221 J g^{-1} . Therefore, TPU auxetic structures are the potential candidate for cyclic loading with relatively high displacement for dissipation energy application.

4.3. Experimental and Numerical Results for PA 12

This section examines 3D-printed PA 12 auxetic structures under displacement-controlled loading. The behaviors of PA 12 auxetic structures during different stages of the loading–unloading process are presented in Figure 9 at the displacement of 9 mm. As has been discussed in Section 3, for PA 12 auxetic simulation, an elastic–plastic model is implemented. According to the experimental observation, fracture occurs in the structures after a specified displacement. In this regard, the damage is modeled in the FEM. To model the damage based on the elastic–plastic behavior of PA 12, the ductile damage is defined in ABAQUS software. The fracture energy of PA 12 is used from available experimental data.^[45] The required data are listed in Table 2. ABAQUS can predict the fracture using the ductile damage initiation criterion (DUCTCRT). The DUCTCTR ranges from 0 to 1. When it reaches 1, the damage initiates, and the material loses its load-carrying capacity.

Figure 9 presents the location of cracks both in the experimental observation and numerical modeling. As shown in Figure 9, the FEM can predict the location of cracks with acceptable accuracy. The green circles show locations accurately detected by numerical modeling; in contrast, the red circle shows dissimilarity in crack location between numerical and experimental results. Indeed, it is possible that the crack has initiated in the red circle but cannot be seen by the naked eye. To present the locations of elements that lost their load-carrying capacity (where cracks occur) by FEM, the DUCTCRT contour is set to only show

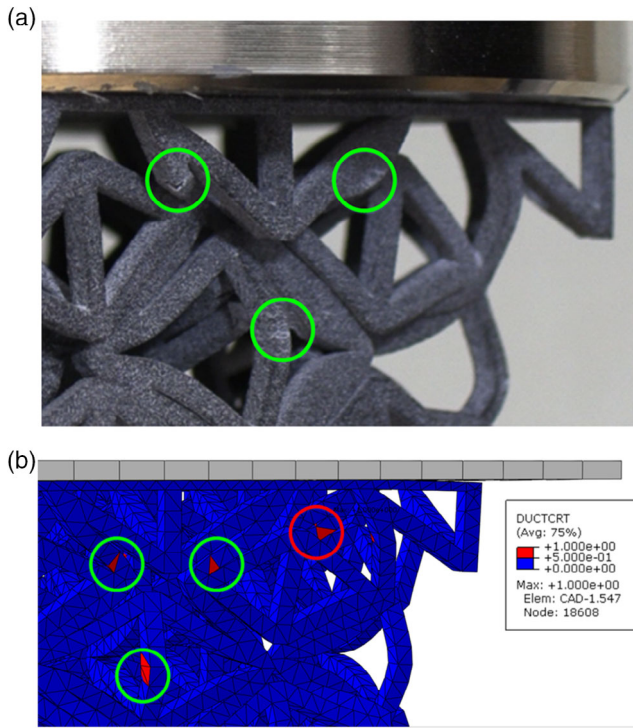


Figure 9. Crack location for PA 12 meta-structure at the displacement of 9 mm: a) experimental observation, b) FEM prediction.

Table 2. Damage modeling parameters of PA 12.

Fracture strain	Fracture energy [$\text{m} \text{mm}^{-2}$] ^[45]	Stress triaxiality
0.23	0.8	0.33

elements that reach the maximum value (1) (therefore, the DUCTCRT of elements less than 1 is shown in blue).

The following data examines the mechanical behavior of PA 12 meta-structure under cyclic loading. Different strains (\approx displacements) are applied to the upper movable jaw to investigate the response of PA 12 auxetic structures to the cyclic loading. **Figure 10a–c** shows the PA 12 auxetic structure configuration at the rest condition, maximum loading, and unloading related to the 11th cycle. As illustrated in Figure 10b, densification occurs at the middle line of the structure. In this area, the beam-like members contact each other, which increases the load. At the end of unloading (see Figure 10c), the structure cannot fully recover to its initial shape due to residual plastic strains, especially in the middle line section. Figure 10d–f presents the deformation at different stages predicted by the FEM simulation. As can be seen, the simulation predicts the deformation in the structure very close to the experimental configuration. Figure 10f illustrates the final stage of the cycle, the end of unloading. It is found that the residual stress is higher in the middle line of the structure (see stress contour).

Figure 11 illustrates the configuration of the PA 12 auxetic structure before and after the 12th loading cycle with a maximum displacement of 15 mm (until failure). In this test, the loading is applied until the failure of the structure happens. Figure 11a demonstrates the start of loading, which is applied after cycle 11. Figure 11b shows the final form of the structure at the end of loading and after the failure. The location of cracks in the structure in an isometric view is presented in Figure 11c. FEM simulation results are presented in Figure 11d–f. As shown by both simulation and experiments, the structure is auxetic and compressed at the middle line under compression loading. As indicated in Figure 11e, the maximum stress occurs in the middle line, which leads to failure in this area. Figure 11f presents the locations of cracks predicted by FEM; some of these cracks cannot be seen in the experiment by the naked eye (see Figure 11c).

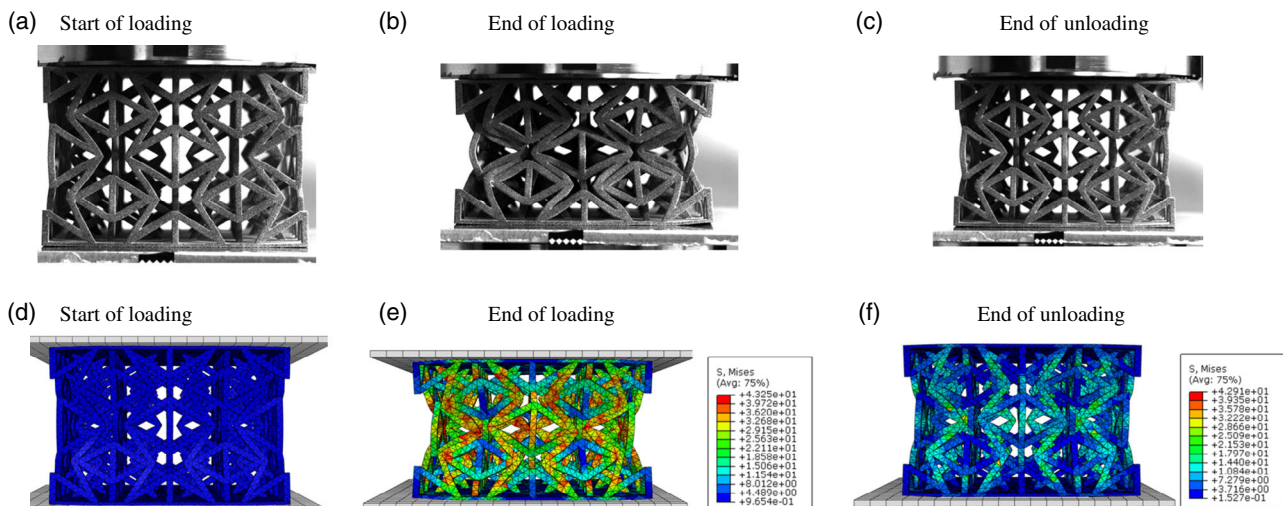


Figure 10. Deformation of PA 12 auxetic meta-structure under the 11th loading–unloading cycle with a maximum displacement of 9 mm: a) start of loading (experiment), b) end of loading (experiment), c) end of unloading (experiment), d) start of loading (simulation), e) end of loading (simulation), f) end of unloading (simulation).

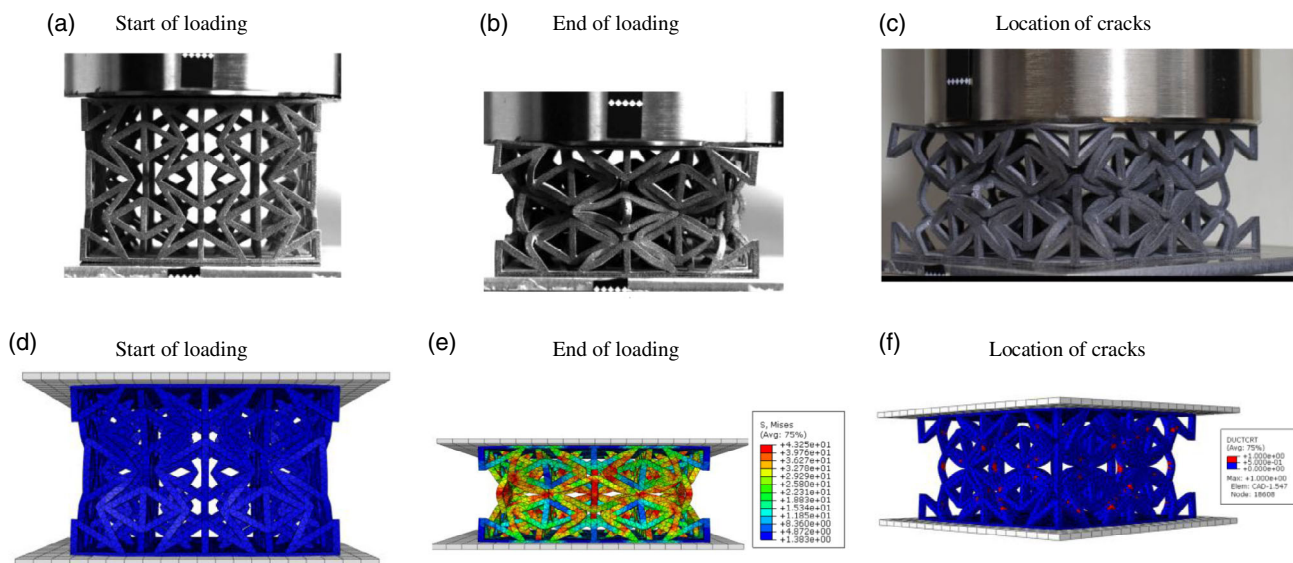


Figure 11. Deformation of PA 12 auxetic meta-structure under the loading step of the 12th cycle with a maximum displacement of 15 mm (until failure): a) start of loading (experiment), b) end of loading (experiment), c) location of cracks (experiment), d) start of loading (simulation), e) end of loading (simulation), f) location of cracks (simulation).

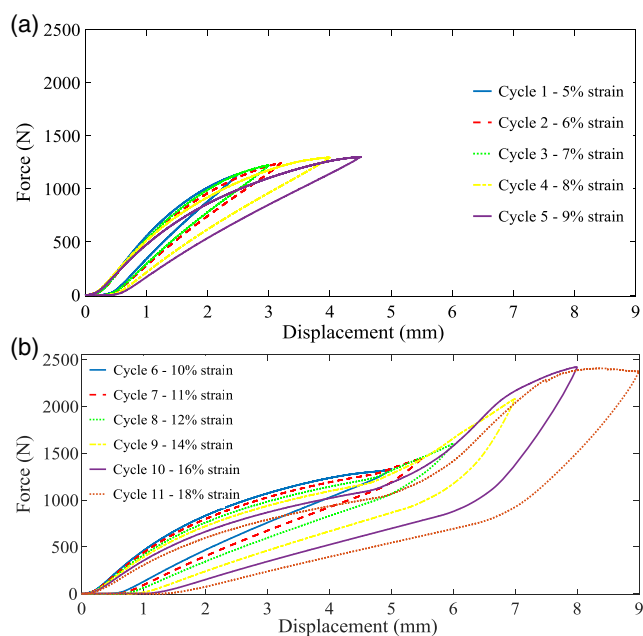


Figure 12. Experimental force–displacement response of PA 12 meta-structure at different cycle: a) from cycle 1 to cycle 5, b) from cycle 6 to cycle 11.

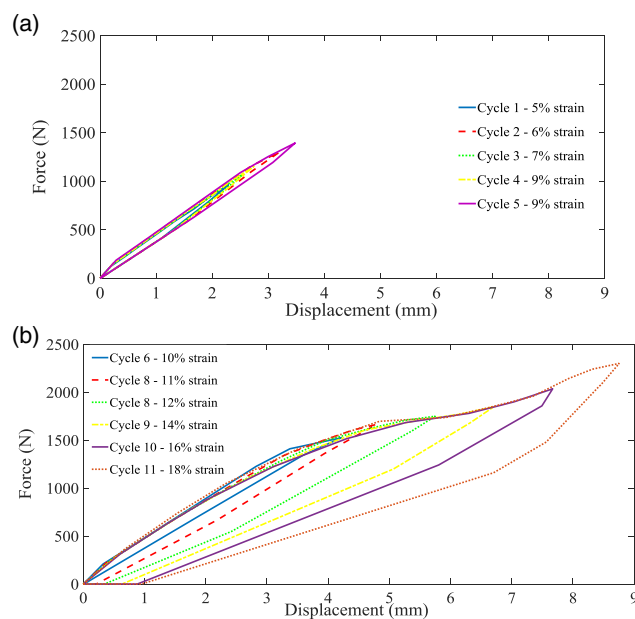


Figure 13. The counterparts of Figure 12 predicted by FEM.

In **Figure 12**, the experimental force–displacement response for different cyclic loadings from cycle 1 to cycle 11 applied to PA 12 auxetic structure is presented. **Figure 13** shows the numerical load–displacement response of PA 12 auxetic structures subjected to different loading cycles predicted by FEM. The preliminary conclusion drawn from Figures 12 and 13 is that FEM can predict experimental results with a high accuracy.

There is a good correlation between experimental and numerical curves verifying the capability of the developed FEM in replicating softening and hardening, the evolution of stress hysteresis, loop area, and the evolution of residual plastic deformations with the number of cycles. As indicated in Figure 12, for cycle 10 as an example, at the first loading stage (0–2 mm), the load versus displacement has a linear elastic behavior; after that, the middle line structure is compressed, and the V-shaped beam-like members bend. Between displacements 2 and –5 mm, the plateau regime

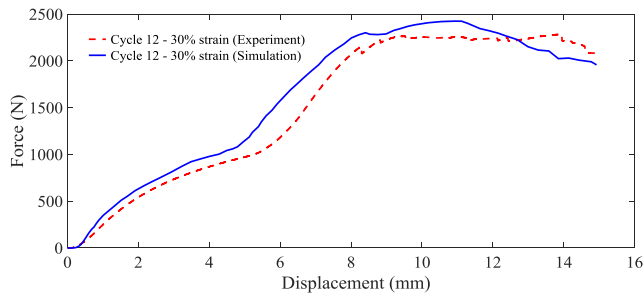


Figure 14. Experimental and numerical force–displacement response of PA 12 meta-structure at the 12th loading cycle.

can be seen (with a slight slope), in which the displacement increases at a high rate almost at the same load. At the displacement range of 5–8 mm, densification occurs, so the slope of the load–displacement curve increases. Afterward, the unloading is followed, and the structure tends to recover its initial shape; however, partial shape recovery is observed due to the residual plastic strain.

To further compare the experimental and numerical results, force–displacement for cycle 12 which leads to failure is illustrated in **Figure 14**. To achieve better simulation results and to increase the number of points in which the ABAQUS reports load and displacement for the reference point of the rigid upper jaw, the number of step increments is increased. It should be mentioned that this option increases the computing time and the output size. As seen in **Figure 14**, FEM can predict the force–displacement response and the failure.

4.4. Dissipated and Absorbed Energies, and SEA for PA 12

The values of dissipated energy, absorbed energy, and SEA for both PA 12 samples predicted by FEM are listed in **Table 3**. Based on the results by increasing the strain, the SEA increases as well. Cycle 12 has the maximum SEA, which is 0.616 J g^{-1} . In this cycle, failure occurs, and the structure dissipates the most

Table 3. Dissipated energy, absorbed energy, and SEA for PA 12 auxetic meta-structure.

Cycle	Dissipated energy [J]	Absorbed energy [J]	SEA [J g^{-1}]
Cycle 1	0.355	1.220	0.009
Cycle 2	0.492	1.631	0.013
Cycle 3	0.618	2.125	0.0158
Cycle 4	0.869	2.408	0.022
Cycle 5	1.031	2.682	0.026
Cycle 6	1.265	3.010	0.032
Cycle 7	1.508	3.311	0.039
Cycle 8	1.760	3.647	0.045
Cycle 9	2.740	4.352	0.070
Cycle 10	3.966	5.072	0.102
Cycle 11	5.284	5.464	0.135
Cycle 12	24.13	0	0.616

energy compared to the other cycles. Moreover, from cycles 1 to 11, the total SEA is 0.509 J g^{-1} ; added to the one for cycle 12, it becomes 1.125 J g^{-1} which is a considerable increase.

4.5. Effect of Auxetic Structures Thickness on the SEA

The effect of the auxetic structure's thickness is another crucial parameter that is investigated in this section. The thickness of the 3D-printed auxetic structure investigated in the previous sections, is 2 mm. By employing the developed FEM, the effect of decreasing and increasing thickness is examined. **Figure 15a–c** presents auxetic structures with 1, 2, and 3 mm thicknesses. As discussed in Section 4, PA 12 auxetic structure under severe loading conditions (30% strain) leads to failure with maximum SEA. Therefore, for the thickness of 1 mm and 3 mm, the structures are subjected to the displacement of 15 mm (30% strain). **Figure 15d–f** presents the deformed auxetic structures with 1, 2, and 3 mm thickness, respectively.

Figure 16 demonstrates the force–displacement response of PA 12 auxetic structures for different thicknesses with a maximum strain of 30%. The presented results reveal that the thickness has an important influence on the mechanical behavior of the meta-structures. It is seen that increasing the thickness from 1 to 3 mm increases the force significantly.

When the force peaks in the force–displacement curve, the fracture is initiated. It is worth mentioning that the fracture occurs for two structures with a thickness of 2 and 3 mm, while it does not happen for a thickness of 1 mm for a strain of 30%. In addition, the fracture in structures with higher thickness occurs at a lower displacement. For example, it is seen that the structure with a thickness of 3 mm experiences fractures at the displacement of 7.8 mm, while the structure with a thickness of 2 mm, it initiates at the displacement of 10 mm.

The dissipated energy, absorbed energy, and SEA for different thicknesses of PA 12 meta-structure under a maximum strain of 30% are presented in **Table 4**. As can be seen, the SEA for the auxetic structure with a thickness of 3 mm is the maximum. Moreover, the structure with a thickness of 1 mm could be used for applications in which structures are subjected to large deformations, and fractures are undesirable.

To make the presentation and compression of SEA calculated for different samples clear, all data listed in **Table 1, 3, and 4** are presented in **Figure 17a–c**, respectively, in a graphical manner.

As mentioned before, one of the important features of the present design is superior SEA capability. In this regard, the maximum SEA determined is 1.06 J g^{-1} compared to common 3D-printed sandwich structures. For example, SEA for triangular corrugated structures^[46] made of unreinforced nylon (PA) and short carbon fiber (SCF) reinforced PA is 0.653 and 0.72 J g^{-1} , respectively. Therefore, SEA in the present design increases by 62% and 47% compared to unreinforced nylon (PA), and SCF reinforced PA triangular corrugated structures. Moreover, the present structure has higher SEA compared to sandwich structures with repairable cores based on truncated cube cells.^[3]

The maximum SEA determined for sandwich structures with repairable cores based on truncated cube cells is 1.05 J g^{-1} ,^[3] while the maximum SEA calculated in the present study is 1.06 J g^{-1} which is a bit higher.

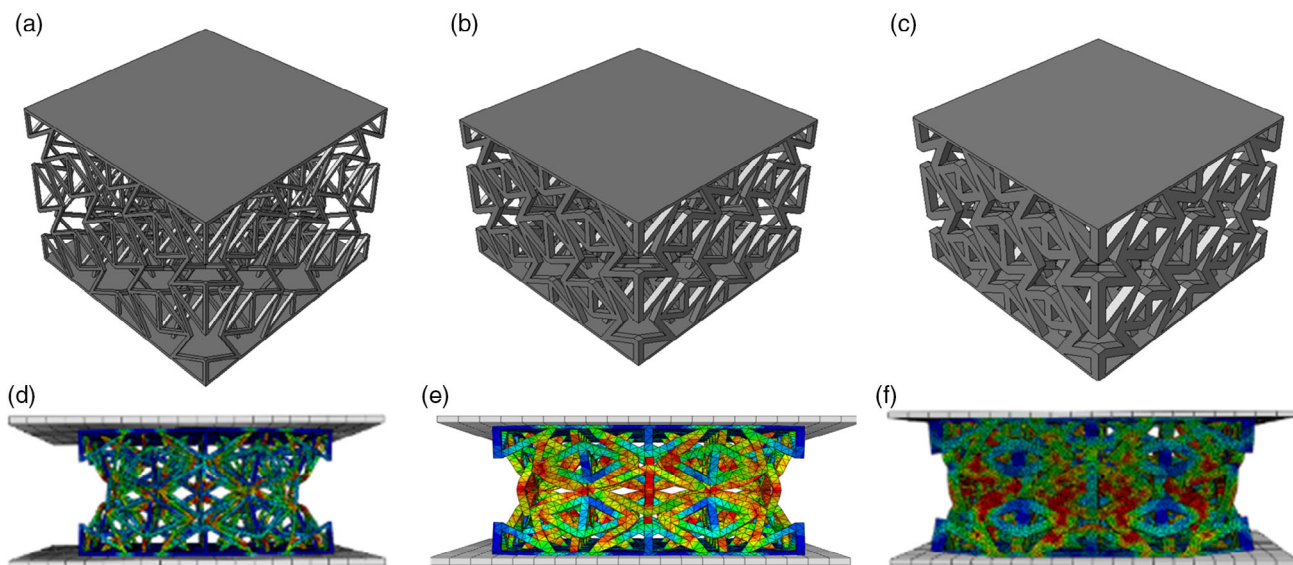


Figure 15. PA 12 auxetic structures with different thicknesses of: a) 1 mm, b) 2 mm, c) 3 mm, and deformed auxetic structures with different thicknesses of: d) 1 mm, e) 2 mm, f) 3 mm.

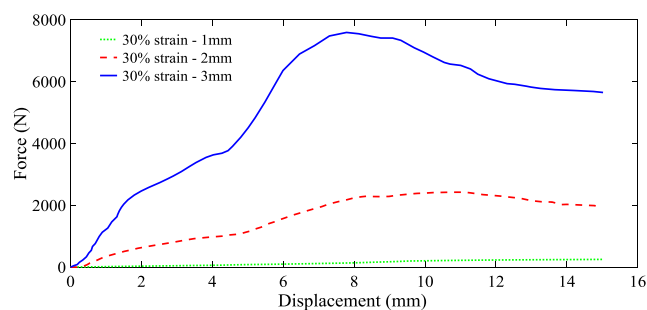


Figure 16. Numerical force–displacement response of PA 12 auxetic structures with different thicknesses.

Table 4. Dissipated energy, absorbed energy, and SEA for PA 12 auxetic structures with different thicknesses.

Samples thickness [mm]	Dissipated energy [J]	Absorbed energy [J]	SEA [J g^{-1}]
1	2.03	0	0.116
2	24.13	0	0.616
3	77.311	0	1.06

4.6. Poisson's Ratio of TPU and PA 12 Auxetic Structures

The Poisson's ratio of both TPU and PA 12 auxetic structures with a thickness of 2 mm is calculated using the FEM. In this regard, the lateral strain is determined by measuring the lateral displacement of the star point in the middle line multiplied by 2 (the displacement of the other side must be calculated too, which is almost the same as the displacement of the star point side,

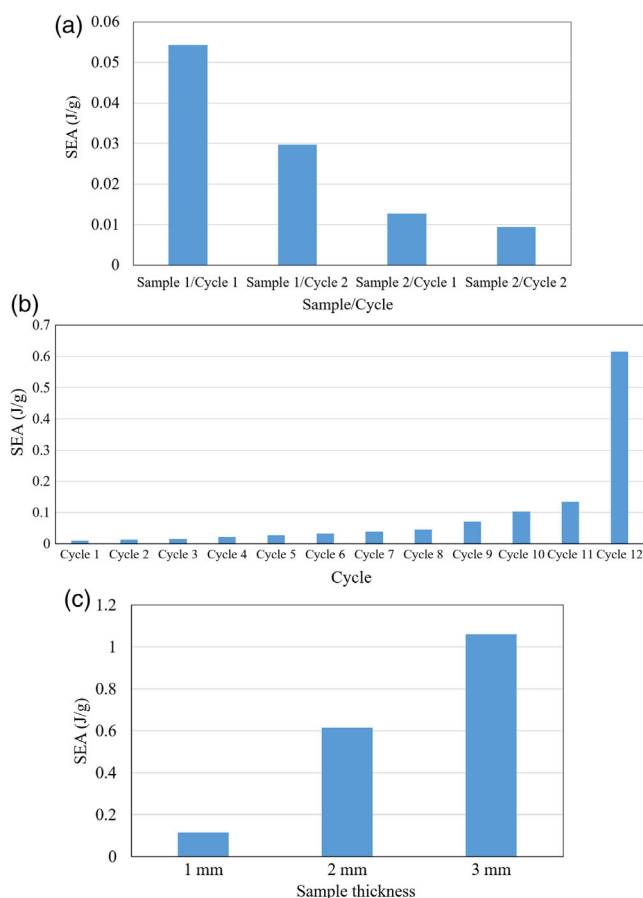


Figure 17. Graphical representation of specific energy absorption (SEA) for: a) TPU (thickness of 2 mm), b) PA 12 (thickness of 2 mm), c) PA 12 (thickness of 1, 2, and 3 mm) samples.

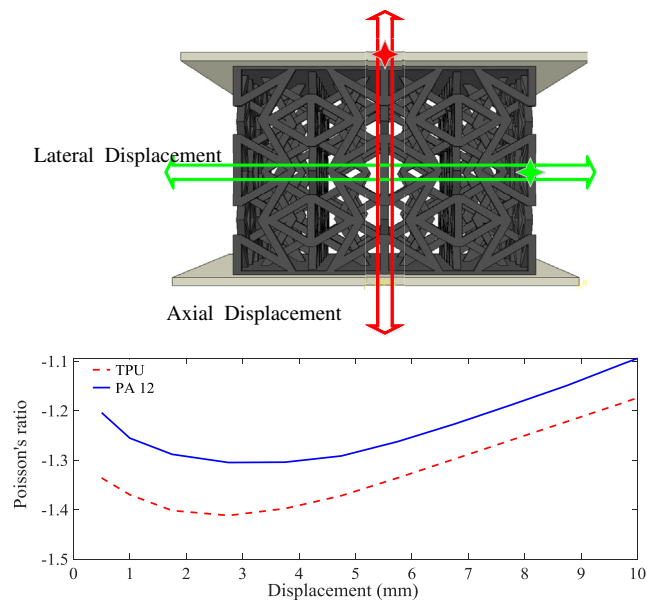


Figure 18. Numerical Poisson ratio versus displacement for TPU and PA 12.

therefore it is multiplied by 2) divided by the width of the structure (77 mm), see **Figure 18a**. It is worth mentioning that 100 elements are considered, and the average displacement is determined for the lateral displacement. Also, the axial strain is the displacement of the upper movable jaw divided by the structure's height (53 mm). The Poisson's ratio is defined as

$$\nu_{xy} = -\frac{\varepsilon_{\text{Lateral}}}{\varepsilon_{\text{Axial}}} \quad (2)$$

Figure 18b presents the Poisson's ratio for both TPU and PA 12 auxetic structures for displacement between 0.5 and 10 mm for the strain of 30%. A similar increasing–decreasing trend in the absolute value of Poisson's ratio is observed for both materials versus the displacement application. As shown in **Figure 18b**, Poisson's ratio of TPU is always higher than PA 12, which is interesting. The main reason could be due to the soft behavior of TPU, which can be compressed in the middle line easier than PA 12. It is also seen that the maximum absolute value of Poisson's ratio occurs at a similar displacement of around 2.75 mm for both materials. The maximum absolute Poisson's ratio for PA 12 and TPU reads -1.30 and -1.41 , proving that the novel proposed designs have an acceptable high auxeticity.

5. Conclusion

The present research was dedicated to exploring novel 3D energy-absorbing meta-structures manufactured by MJF 3D printing technology. The concept was based on arranging unit cells of soft hyper-elastic TPU and hard elastoplastic PA 12 to engineer high-performance auxetic structures under cyclic loadings. The FEM was developed using ABAQUS to accurately simulate the highly nonlinear behaviors of the 3D-printed meta-structures under compressive loading–unloading cycles.

The feasibility and mechanical performance of the meta-structures were assessed experimentally and numerically. The TPU auxetics were shown to possess stress softening, hysteresis, cyclic stress softening, and high energy absorption/dissipation, while PA 12 revealed elastoplastic behaviors with some residual strains and supreme energy absorption/dissipation performance. Comparative studies revealed that the key aspects of meta-structures were well simulated in capturing stress softening/hardening, plateau during hyper-elasticity and plasticity, plastic deformation growth, unloading path, Mullin effect, cyclic stress softening, hysteresis area, fracture, and residual strain. Finally, the following concluding remarks can be summarized: 1) The proposed structure is auxetic and has a negative Poisson ratio; 2) TPU auxetic structures withstand large deformation and can recover their initial form even after a strain of 50%; 3) PA 12 auxetic structures withstand higher load and lower displacement compared to TPU auxetic structures; 4) The SEA (also dissipated energy) of the TPU auxetic structure decreases by 45% in cycle 2 compared to cycle 1; 5) Cycle 12th loading of PA 12 (a strain of 30%) leads to failure and the maximum SEA; 6) PA 12 auxetic structures with a thickness of 3 mm have a maximum SEA of 1.06 J g^{-1} . Also, by increasing the thickness, the fracture occurs at lower displacements. Moreover, the fracture does not happen in a structure with a thickness of 1 mm for a displacement of 15 mm; 7) TPU auxetic structures have a higher Poisson's ratio, which is due to the soft behavior of TPU.

Due to the absence of similar concepts and results in the specialized literature, this article advances the state-of-the-art 3D printing meta-structures with high energy absorption/dissipation features for impact protection and shock mitigation applications.

Acknowledgements

The authors gratefully acknowledge use of the services and facilities at Nottingham Trent University.

Conflict of Interest

The authors declare no conflict of interest.

Data Availability Statement

All data are presented in the article.

Keywords

3D printing, meta-materials, polymers, snowflake-inspired design, stress softening

Received: August 17, 2022
Revised: November 20, 2022
Published online:

- [1] R. Johnston, Z. Kazanci, *Addit. Manuf.* **2021**, *38*, 101783.
[2] M. Safarabadi, M. Haghghi-Yazdi, M. A. Sorkhi, A. Yousefi, *J. Sandwich Struct. Mater.* **2021**, *23*, 3985.

- [3] R. Hedayati, A. Yousefi, M. Bodaghi, *Composites, Part B* **2022**, *243*, 110124.
- [4] A. Alomarah, S. H. Masood, I. Sbarski, B. Faisal, Z. Gao, D. Ruan, *Virtual Phys. Prototyping* **2020**, *15*, 1.
- [5] M. J. Mirzaali, H. Pahlavani, E. Yarali, A. A. Zadpoor, *Sci. Rep.* **2020**, *10*, 1.
- [6] K. E. Evans, *Endeavour* **1991**, *15*, 170.
- [7] D. Li, L. Dong, R. S. Lakes, *Phys. Status Solidi B* **2013**, *250*, 1983.
- [8] I. I. Argatov, R. Guinovart-Díaz, F. J. Sabina, *Int. J. Eng. Sci.* **2012**, *54*, 42.
- [9] M. Bianchi, F. L. Scarpa, C. W. Smith, *J. Mater. Sci.* **2008**, *43*, 5851.
- [10] J. B. Choi, R. S. Lakes, *J. Mater. Sci.* **1992**, *27*, 4678.
- [11] G. Imbalzano, P. Tran, T. D. Ngo, P. V. S. Lee, *Compos. Struct.* **2016**, *135*, 339.
- [12] J. Simpson, Z. Kazanci, *Thin-Walled Struct.* **2020**, *150*, 106676.
- [13] J. Zhang, G. Lu, Z. You, *Composites, Part B* **2020**, *201*, 108340.
- [14] S. Bronder, F. Herter, A. Röhrig, D. Bähre, A. Jung, *Adv. Eng. Mater.* **2022**, *24*, 2100816.
- [15] C. R. De Lima, G. H. Paulino, *Adv. Eng. Software* **2019**, *129*, 69.
- [16] K. E. Evans, A. Alderson, *Adv. Mater.* **2000**, *12*, 617.
- [17] G. Imbalzano, S. Linforth, T. D. Ngo, P. V. S. Lee, P. Tran, *Compos. Struct.* **2018**, *183*, 242.
- [18] X. Ren, R. Das, P. Tran, T. D. Ngo, Y. M. Xie, *Smart Mater. Struct.* **2018**, *27*, 023001.
- [19] M. Wallbanks, M. F. Khan, M. Bodaghi, A. Triantaphyllou, A. Serjouei, *Smart Mater. Struct.* **2021**, *31*, 023002.
- [20] M. Kowalska, M. Woźniak, M. Kijek, P. Mitrosz, J. Szakiel, P. Turek, *Sci. Rep.* **2022**, *12*, 1.
- [21] D. Photiou, S. Avraam, F. Sillani, F. Verga, O. Jay, L. Papadakis, *Appl. Sci.* **2021**, *11*, 10362.
- [22] H. Rahman, E. Yarali, A. Zolfagharian, A. Serjouei, M. Bodaghi, *Materials*, **2021**, *14*, 1366.
- [23] N. K. Choudhry, B. Panda, S. Kumar, *Composites, Part B* **2022**, *228*, 109437.
- [24] S. Gohar, G. Hussain, M. Ilyas, A. Ali, J. Mater. Res. Technol. **2021**, *15*, 394.
- [25] Z. Wang, C. Luan, G. Liao, J. Liu, X. Yao, J. Fu, *Adv. Eng. Mater.* **2020**, *22*, 2000312.
- [26] M. Bodaghi, A. Serjouei, A. Zolfagharian, M. Fotouhi, H. Rahman, D. Durand, *Int. J. Mech. Sci.* **2020**, *173*, 105451.
- [27] M. Mehrpouya, A. Gisario, A. Azizi, M. Barletta, *Polym. Adv. Technol.* **2020**, *31*, 3361.
- [28] A. Serjouei, A. Yousefi, A. Jenaki, M. Bodaghi, M. Mehrpouya, *Smart Mater. Struct.* **2022**, *31*, 055014.
- [29] R. Hamzehei, A. Serjouei, N. Wu, A. Zolfagharian, M. Bodaghi, *Adv. Eng. Mater.* **2022**, *24*, 2200656.
- [30] R. Hamzehei, A. Zolfagharian, S. Dariushi, M. Bodaghi, *Smart Mater. Struct.* **2022**, *31*, 035001.
- [31] D. Sharma, S. S. Hiremath, *Compos. Struct.* **2022**, *283*, 115102.
- [32] H. Wang, Z. Huang, J. Li, F. Wang, Z. Feng, H. Tian, H. Zhao, L. Li, *Appl. Phys. Lett.* **2021**, *118*, 131903.
- [33] M. Mehrpouya, T. Edelijin, M. Ibrahim, A. Mohebsshahedin, A. Gisario, M. Barletta, *Adv. Eng. Mater.* **2022**, *24*, 2200677.
- [34] A. Alomarah, S. H. Masood, D. Ruan, *Adv. Eng. Mater.* **2022**, *24*, 2101811.
- [35] S. A. S. A. Saufi, M. Y. M. Zuhri, M. Lalegani, Dezaki, S. M. Sapuan, R. A. Ilyas, A. As'Arry, M. K. A. Ariffin, M. Bodaghi, *Polymers* **2021**, *13*, 4388.
- [36] S. Yuan, F. Shen, J. Bai, C. K. Chua, J. Wei, K. Zhou, *Mater. Des.* **2017**, *120*, 317.
- [37] stratasy, Aurora Flight Sciences Designs and Develops the World's First 3D Printed Jet-Powered Aircraft, **2022**, <https://www.stratasy.com/en/resources/case-studies/aurora/> (accessed: January 2022).
- [38] Standard, A., *D695: Standard Test Method for Compressive Properties of Rigid Plastics*, ASTM International, West Conchohocken **2008**.
- [39] International, A., *ASTM D638-14, Standard Test Method For Tensile Properties Of Plastics*, ASTM International, West Conshohocken, PA **2015**.
- [40] L. Mullins, *Rubber Chem. Technol.* **1948**, *21*, 281.
- [41] L. Wei, X. Zhao, Q. Yu, G. Zhu, *Thin-Walled Struct.* **2020**, *149*, 106623.
- [42] X. Zhao, L. Wei, D. Wen, G. Zhu, Q. Yu, Z. D. Ma, *Eng. Struct.* **2021**, *247*, 113204.
- [43] E. Yarali, R. Noroozi, A. Yousefi, M. Bodaghi, M. Baghani, *Polymers* **2020**, *12*, 489.
- [44] S. Cantournet, R. Desmorat, J. Besson, *Int. J. Solids Struct.* **2009**, *46*, 2255.
- [45] J. Fonseca, I. A. Ferreira, M. F. S. F. De Moura, M. Machado, J. L. Alves, *Compos. Struct.* **2019**, *214*, 316.
- [46] B. Wang, Y. Ming, J. Zhou, H. Xiao, F. Wang, Y. Duan, Z. Kazanci, *Polym. Test.* **2022**, *106*, 107469.